

Time-resolved thermal lens investigation of glassy dynamics in supercooled liquids: Theory and experiments

Pengfei Zhang, Marco Gandolfi, Francesco Banfi, Christ Glorieux, Liwang Liu

▶ **To cite this version:**

Pengfei Zhang, Marco Gandolfi, Francesco Banfi, Christ Glorieux, Liwang Liu. Time-resolved thermal lens investigation of glassy dynamics in supercooled liquids: Theory and experiments. Journal of Chemical Physics, 2021, 155 (7), pp.074503. 10.1063/5.0060310 . hal-03327275

HAL Id: hal-03327275
https://hal.science/hal-03327275

Submitted on 27 Aug 2021

HAL is a multi-disciplinary open access archive for the deposit and dissemination of scientific research documents, whether they are published or not. The documents may come from teaching and research institutions in France or abroad, or from public or private research centers.

L'archive ouverte pluridisciplinaire **HAL**, est destinée au dépôt et à la diffusion de documents scientifiques de niveau recherche, publiés ou non, émanant des établissements d'enseignement et de recherche français ou étrangers, des laboratoires publics ou privés.

The Journal of Chemical Physics ARTICLE scitation.org/journal/jcp

Time-resolved thermal lens investigation of glassy dynamics in supercooled liquids: Theory and experiments

Cite as: J. Chem. Phys. 155, 074503 (2021); doi: 10.1063/5.0060310
Submitted: 17 June 2021 • Accepted: 3 August 2021 •
Published Online: 18 August 2021

View Online Export Citation CrossMark

Pengfei Zhang,[1] Marco Gandolfi,[1,2,3,4] Francesco Banfi,[5] Christ Glorieux,[1] and Liwang Liu[1,a)]

AFFILIATIONS

[1] Laboratory for Soft Matter and Biophysics, Department of Physics and Astronomy, KU Leuven, Celestijnenlaan 200D, B-3001 Heverlee, Belgium
[2] CNR-INO, Via Branze 45, 25123 Brescia, Italy
[3] Department of Information Engineering, University of Brescia, Via Branze 38, 25123 Brescia, Italy
[4] Dipartimento di Matematica e Fisica, Università Cattolica del Sacro Cuore, Via Musei 41, 25121 Brescia, Italy
[5] FemtoNanoOptics Group, Université de Lyon, CNRS, Université Claude Bernard Lyon 1, Institut Lumière Matière, F-69622 Villeurbanne, France

[a)] **Author to whom correspondence should be addressed:** liwang.liu@kuleuven.be

ABSTRACT

This work reports results on the simultaneous spectroscopy of the specific heat and thermal expansivity of glycerol by making use of a wideband time-resolved thermal lens (TL) technique. An analytical model is presented which describes TL transients in a relaxing system subjected to impulsive laser heating. Experimentally, a set of TL waveforms, from 1 ns to 20 ms, has been recorded for a glycerol sample upon supercooling, from 300 to 200 K. The satisfactory fitting of the TL signals to the model allows the assessment of relaxation strength and relaxation frequency of the two quantities up to sub-100 MHz, extending the specific heat and thermal expansion spectroscopy by nearly three and eight decades, respectively. Fragility values, extracted from the relaxation behavior of the specific heat and the thermal expansion coefficient, are found to be similar, despite a substantial difference in relaxation strength.

Published under an exclusive license by AIP Publishing. https://doi.org/10.1063/5.0060310

I. INTRODUCTION

Upon cooling below the freezing point, most liquids can avoid crystallization,[1,2] provided the cooling takes place sufficiently fast, and reach a metastable glassy state. This phenomenon, i.e., supercooling or undercooling, has been at the forefront of condensed matter research for decades[3–6] owing to its impact on various branches of science and technology, e.g., energy storage,[7] food manufacturing,[8] and pharmaceutical development.[9] Supercooled materials exhibit a frequency-dependent response to different kinds of stimuli.[10–12] The most direct manifestation of this feature is expressed in the frequency dependence of the elastic moduli of such relaxing systems, which behave more rigidly upon faster stimulation due to a decreasing number of possibilities for cooperative molecular motions within an oscillation period. The characteristic relaxation frequency, i.e., the frequency below which the system behaves substantially more softly than in the high-frequency limit, drastically decreases with decreasing temperature.[13,14] In the so-called strong glasses, the temperature dependence of the relaxation frequency follows an Arrhenius law. In the so-called fragile systems, the Arrhenius plot is curved. The degree of temperature variation of its slope, which is proportional to the activation energy of the related process (e.g., mechanical compression), is quantified by the so-called fragility.[15] As the temperature dependence of the relaxation dynamics is strong,[3] many attempts have been made to develop and combine different experimental approaches to address the relaxation dynamics in a broad frequency range. Dielectric spectroscopy and mechanical spectroscopy[13] are the most frequently used techniques owing to their extraordinary bandwidth, covering 18[16] and 13 decades,[17]

Published under an exclusive license by AIP Publishing

respectively, and enabling the test of several key predictions and models developed in glass physics across a wide temperature range, e.g., time–temperature superposition,[18,19] power law,[20] or mode-coupling theory.[21–23] Along with dielectric and mechanical relaxation, thermal relaxation[19,24,25] has also proven to be valuable to investigate as it is closely tied with the thermodynamics of the system. Specifically, thermal relaxation is believed to couple all degrees of freedom equally, which is not the case for dielectric or mechanical relaxation that couples mainly rotational or translational motions, respectively.[26,27] In practice, thermal relaxation has been observed as a frequency dependence of the specific heat capacity $C(\omega)$ through the 3-ω technique,[27,28] photopyroelectric spectroscopy (PPE),[29,30] and AC-chip nano-calorimetry,[31] and of the thermal expansion coefficient $\gamma(\omega)$ through capacitive scanning dilatometry.[32,33] However, until now, the possibility of thermal relaxation has been comparatively much less exploited because of the narrow frequency range that could be experimentally covered by thermal response techniques, about 100 kHz for specific heat spectroscopy[29,30] and only 1 Hz for thermal expansivity spectroscopy.[32,33] Interestingly, it has been observed in some glass formers that the rotational motion slows down more dramatically than the translational motion,[34,35] namely, the so-called time-scale decoupling.[19,36] Thermal relaxation couples all motions and weights all degrees of freedom in the liquid equally, which raises the question of whether such features are also manifest in the thermal relaxation dynamics, which reflect the combined energetic impact of all motional (translational, shear, rotational, and vibrational) degrees of freedom. In particular, it would be interesting to verify whether the fragility and the temperature dependence of the relaxation frequency (see below for the quantitative definition) of the heat capacity are consistent with the ones measured via other susceptibilities.

In this work, we report on the broadband spectroscopy of $C(\omega)$ and $\gamma(\omega)$ all the way to sub-100 MHz exploiting time-resolved thermal lens (TL) spectroscopy in which the transient density or strain response of a relaxing sample, triggered by a short pulse laser heating, is exploited to investigate the structural relaxation behavior. The detailed theoretical modeling of the time-resolved TL signals in a relaxing system is presented. An experimental TL spectroscopy of the thermal relaxation dynamics, $C(\omega)$ and $\gamma(\omega)$, in supercooled glycerol is illustrated. Key relaxation features, e.g., low/high-frequency limit response, relaxation strength, and characteristic frequencies, are determined and compared with those of mechanical and dielectric relaxation as determined by other techniques.

This article is structured as follows: In Sec. II, we present the modeling of the TL response in a glassy system, starting with the calculation of the temperature response, initiated by the impulsive photothermal excitation, to the derivation of thermoelastic coupling in a relaxing system. Finally, an analytical expression to describe the time-resolved TL response based on Fourier optics is proposed. Section III shows the experimental TL spectroscopy of the slowing glassy dynamics in supercooled glycerol. The model developed in this work is deployed to extract $C(\omega)$ and $\gamma(\omega)$ in a board frequency range, from sub-kilohertz to tens of MHz, and in a wide temperature range from 200 to 300 K. Conclusions and perspectives of the approach are given in Sec. IV.

II. MODELING OF THE TL RESPONSE IN A RELAXING SYSTEM

TL spectroscopy is a photothermal method that detects the temperature variation in a sample due to heat generated from non-radiative relaxation processes resulting from the optical absorption of light.[37] It has been widely used for the thermo-optical characterization of materials, spectrometry of photochemical reactions, and trace analyses of gas and liquids.[38–42] This work extends its application to the spectroscopy of glassy dynamics, focusing on the relaxation of specific heat and thermal expansivity. We start with the theoretical modeling of the time-resolved TL response in a relaxing system.

Figure 1 shows a typical beam geometry in TL experiments, in which coaxially aligned pump (red) and probe (green) laser beams are focused into the bulk of a weakly absorbing sample that is sealed in a cuvette. Local photothermal heating near the pump beam waist produces a transverse temperature gradient and gives rise to a refractive index gradient and hence a TL (gradient-index). The TL may behave like a concave or a convex lens, depending on the thermo-optical coefficient of the sample, which perturbs the wavefront of the propagating probe beam, e.g., beam divergence. The rationalization of the experiments can be achieved with the following three steps: In the first step (A), the temperature distribution in the sample is calculated; in the second step (B), the strain response, caused by the thermally induced radial strain, namely, a combination of the thermal strain and acoustic strain, is derived; and in the third step (C), the optical far-field variation is calculated based on Fourier optics.

A. Photothermally induced temperature field in a relaxing system

Given a weakly absorbing material, in a TL experiment scheme, the heat distribution along the (collinear) pump and probe beam direction or the z-direction can be considered uniform since the axial distance over which the probe beam interacts with the sample is much shorter than the optical penetration depth. The temperature field then depends only on the radial direction. The heat diffusion equation can be written in cylindrical coordinates as[43,44]

$$\frac{1}{r}\frac{\partial}{\partial r}\left(r\frac{\partial \Delta T(r,t)}{\partial r}\right)-\frac{1}{\alpha}\frac{\partial \Delta T(r,t)}{\partial t}=-\frac{Q(r,t)}{\kappa}, \tag{1}$$

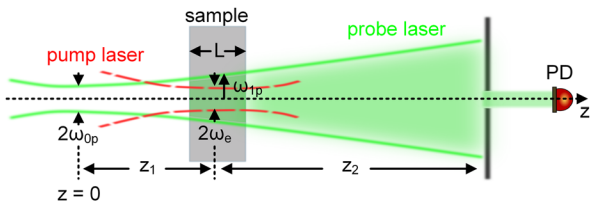


FIG. 1. A schematic diagram of the geometric arrangement of the pump–probe beams in a TL experiment. The position of the probe beam waist, ω_{0p}, is taken as the origin ($z = 0$) along the z-axis. The sample is located at z_1. A focused pump beam of spot size (radius) ω_e is used to photothermally excite the sample, causing the thermal lens effect that perturbs the optical field at the detection plane located at the distance of z_2 from the sample center.

Published under an exclusive license by AIP Publishing

where $\Delta T\ (r = R,\ t) = 0$ is the boundary condition, with R (mm) being the radius of the sample, which also defines the calculation (cylindrical) domain with an artificial boundary condition; $\alpha = \kappa/\rho C$ ($m^2\ s^{-1}$) is the thermal diffusivity; and κ ($W\ m^{-1}\ K^{-1}$), ρ ($kg\ m^{-3}$), and C ($J\ kg^{-1}\ K^{-1}$) are the thermal conductivity, density, and specific heat capacity, respectively. $Q(r, t)$ ($J\ s^{-1}\ m^{-3}$) is the absorbed power density, which, in the case of the TEM00 Gaussian excitation beam, can be expressed, within the paraxial approximation, as[43]

$$Q(r,t) = Q_0\ \exp\left(-\frac{2r^2}{\omega_e^2}\right)\delta(t), \tag{2}$$

where Q_0 ($J\ m^{-3}$) is the supplied heat density. The Dirac delta function in time δ(t) (s^{-1}) accounts for the impulsive excitation. The physical meaning of this condition is that the system is initially at equilibrium, i.e., $\Delta T\ (r,\ t) = 0$ for $t < 0$, and at time $t = 0$, an ultrashort pulse excites the system. After the Fourier transform, the temperature distribution in the frequency domain can be written as

$$\frac{1}{r}\frac{\partial}{\partial r}\left(r\frac{\partial \Delta\tilde{T}(r,\omega)}{\partial r}\right) - \frac{i\omega}{\alpha}\Delta\tilde{T}(r,\omega) = -\frac{Q_0}{2\pi\kappa}\exp\left(-\frac{2r^2}{\omega_e^2}\right), \tag{3}$$

with $i^2 = -1$. Functions defined on a finite interval can be expanded in terms of a Fourier Bessel series.[45] Thus, the solution of Eq. (3) can be written as

$$\Delta\tilde{T}(r,\omega) = \sum_{n=1}^{\infty} J_0(q_n r)\theta_n(\omega), \tag{4}$$

where $q_n = j_{0n}/R$, with j_{0n} denoting the nth root of the zero-order Bessel function of the first kind $J_0(x)$, and $\theta_n(\omega)$ is the corresponding Fourier Bessel coefficients. Inserting Eq. (4) into Eq. (3) (see supplementary material for detailed calculation) yields

$$\sum_{n=1}^{\infty} J_0(q_n r)\theta_n(\omega)\left(\kappa q_n^2 + i\omega\rho C\right) = \frac{Q_0}{2\pi}\exp\left(-\frac{2r^2}{\omega_e^2}\right). \tag{5}$$

Then, the unknown Fourier Bessel coefficients $\theta_n(\omega)$ can be determined by using the orthogonality properties of the Bessel function.[46] Multiplying $rJ_0(q_{n'}r)$ on both sides of Eq. (5) and integrating over r from 0 to R, we obtain

$$\theta_n(\omega) = \frac{Q_0 I_n}{\pi J_1^2(j_{0n})R^2} \times \frac{1}{\kappa q_n^2 + i\omega\rho C}, \tag{6}$$

where $J_1(x)$ is the 1st order Bessel function of the first kind. I_n can be approximated as

$$\begin{aligned} I_n &= \int_0^R \exp\left(-\frac{2r^2}{\omega_e^2}\right)J_0(q_n r)rdr \\ &\approx \int_0^\infty \exp\left(-\frac{2r^2}{\omega_e^2}\right)J_0(q_n r)rdr = \frac{\omega_e^2}{4}\exp\left(-\frac{\omega_e^2 q_n^2}{8}\right). \end{aligned} \tag{7}$$

This approximation is reasonable as the radius of the sample far exceeds the excitation beam waist ($R = 5$ mm and $\omega_e \approx 30\ \mu$m in our experiment). The last equality arises using the Hankel transform of the Gaussian function. In the impulsive stimulated TL experiment of glassy systems, complex frequency-dependent behavior is found for the specific heat capacity. We assume that the thermal conductivity is frequency independent, which has been validated up to kilohertz frequencies,[27,30] although it is unclear to what extent the assumption can still hold. Following the Debye relaxation model, we use

$$C(\omega) = C_\infty + \frac{\Delta C}{1 + i\omega/\omega_C}, \tag{8}$$

where $\Delta C = C_0 - C_\infty$, with C_∞ being the high-frequency limit and C_0 the low-frequency (or static) limit of specific heat capacity, and ω_C (s^{-1}) is the characteristic relaxation (angular) frequency, which strongly depends on temperature. Thus, the final temperature distribution in the frequency domain is obtained by combining the aforementioned relations as follows:

$$\Delta\tilde{T}(r,\omega) = \sum_{n=1}^{\infty} J_0(q_n r)\frac{Q_0 I_n}{\pi\rho C_\infty J_1^2(j_{0n})R^2} \times \frac{-i(\omega - i\omega_C)}{(\omega - \omega_{1n})(\omega - \omega_{2n})}, \tag{9}$$

with

$$\begin{cases} \omega_{1n} = \dfrac{i}{2}\left(q_n^2\alpha + \omega_C/\left(1 - \dfrac{\Delta C}{C_0}\right)\right. \\ \qquad \left. - \sqrt{-4q_n^2\alpha\omega_C + \left(q_n^2\alpha + \omega_C/\left(1 - \dfrac{\Delta C}{C_0}\right)\right)^2}\right), \\ \omega_{2n} = \dfrac{i}{2}\left(q_n^2\alpha + \omega_C/\left(1 - \dfrac{\Delta C}{C_0}\right)\right. \\ \qquad \left. + \sqrt{-4q_n^2\alpha\omega_C + \left(q_n^2\alpha + \omega_C/\left(1 - \dfrac{\Delta C}{C_0}\right)\right)^2}\right), \end{cases} \tag{10}$$

where $\alpha = \alpha_0/(1 - \Delta C/C_0)$, with $\alpha_0 = \kappa/\rho C_0$. The advantage of the notation in Eq. (9) is that it is easily transformed back to the time domain by making use of the residue theorem (see supplementary material B for detailed expression), yielding $\Delta T\ (r, t)$ in terms of the sum of two exponentially damped contributions as follows:

$$\begin{aligned} \Delta T(r,t) = &\sum_{n=1}^{\infty} J_0(q_n r)\frac{2Q_0 I_n}{\rho C_\infty J_1^2(j_{0n})R^2} \\ &\times \left(\frac{(\omega_{1n} - i\omega_C)}{\omega_{1n} - \omega_{2n}}\exp(i\omega_{1n}t) + \frac{(\omega_{2n} - i\omega_C)}{\omega_{2n} - \omega_{1n}}\exp(i\omega_{2n}t)\right)H(t), \end{aligned} \tag{11}$$

where $H(t)$ is the Heaviside step function. If the specific heat capacity is independent of frequency (i.e., $\Delta C = 0$), ω_{1n} and ω_{2n} reduce to $i\omega_C$ and $iq_n^2\alpha_0$, respectively. Then, the expression for temperature reduces to the well-known thermal diffusion equation with $q_n^2\alpha_0$ as the thermal diffusion coefficient as follows:

$$\Delta T(r,t) = \sum_{n=1}^{\infty} J_0(q_n r)\frac{2Q_0 I_n}{\rho C_\infty J_1^2(j_{0n})R^2} \times \exp(-q_n^2\alpha_0 t)H(t). \tag{12}$$

Equation (11) calculates the temperature response induced by Dirac delta laser pulses. By calculating (numerically) the convolution between Eq. (11) and a Gaussian function or rectangular function, one can simulate the temperature response induced by laser pulses

Published under an exclusive license by AIP Publishing

of finite width. The advantage of using the Dirac delta function to describe the laser pulse is that it makes it possible to model the TL response in a completely analytical way, which significantly reduces the computation power in the fitting process. However, the width of laser pulses does pose an upper limit of the experimental accessible bandwidth, as illustrated in Fig. 2, which was simulated based on the parameters listed in Table I.

Note that, in the absence of the diffusion term or by setting $t = 0$ in Eq. (12), the Bessel series corresponds to the Bessel expansion of the spatial part of the heat source. In other words, at $t = 0$, the temperature profile corresponds to the heat source profile. In the presence of thermal diffusion, every Bessel wavenumber component diffuses exponentially with thermal diffusion time $1/q_n^2\alpha_0$.

In the case of a non-relaxing material or a material in which the relaxation time is much shorter or much longer than the time needed for the photothermally deposited heat to diffuse away from the excitation region to the surrounding medium, the two exponentials in Eq. (11) decay with the classical thermal diffusion time $\tau_{TD} = 1/(q^2D)$. D denotes the thermal diffusivity, $D = k/\rho C_{eff}$, with k the thermal conductivity, ρ the density, q the wavenumber of the involved spatial Fourier component of the temperature profile, and C_{eff} an effective value of the specific heat capacity, which is either the low- or high-frequency limit for $\tau_{TD} \gg \tau_C$ or $\tau_{TD} \ll \tau_C$. When the heat capacity relaxation occurs on the time scale of the thermal diffusion, the wash out the deposited heat can only be described by two exponentials with different decay times, expressing the combined effect of two processes: thermal diffusion and material relaxation. Figure 2 illustrates the effect of relaxation in the time domain via the temperature evolution of glycerol after a single laser pulse stimulation in the center of the pump laser beam ($r = 0$). The evolution of the impulse response can be intuitively explained as follows: Initially, the photothermally supplied heat only contributes to the vibrational degrees of freedom, resulting in a large initial temperature rise. In the assumed model, this temperature rise is instantaneous. Note that in reality, the photothermally induced temperature increase occurs on time scales determined by the laser pulse dynamics (in our case: nanosecond range) and by optical phonons (picosecond range). As time increases beyond the relaxation time of cooperative configurational network rearrangements, some of the thermal energy is transferred to irreversible rearrangements of the amorphous network. This goes along with a decrease in energy in the vibrational states and thus a decrease in the experimentally observed temperature. Mathematically, this evolution can be described by an effective,

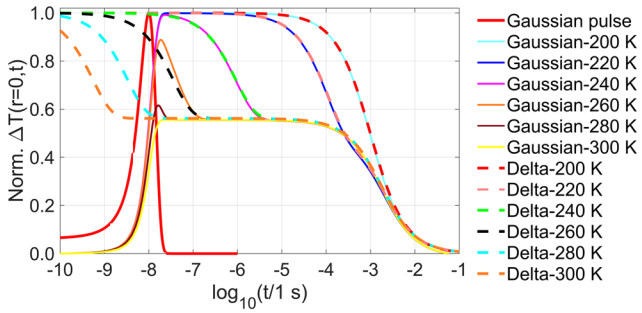


FIG. 2. Simulated normalized temperature response at the focal point of the pump beam (r = 0), with input parameters from glycerol summarized in Table I, plotted on a logarithmic time scale. The normalization was done by dividing the temperature response to its maximum. Two scenarios of simulations are presented: the dashed lines depict the temperature response induced by Dirac delta excitation calculated using Eq. (11), and the solid lines represent the response induced by Gaussian excitation calculated by taking the convolution of Eq. (11) and a Gaussian pulse function, $Q_{Gaussian}(t) = \exp(-2.77[(t - t_0)/\tau_p]^2)$. τ_p is the full-width-at-half-maximum (10 ns here) of the laser pulse, and t_0 is the peak position of the laser pulse (10 ns). Comparison of the two scenarios suggests a mask effect of the finite width of the laser pulse on the relaxation process at a very short time scale (<20 ns), implying that the upper limit of the experimental bandwidth is about sub-100 MHz when using a 10-ns laser as the pump.

instantaneous heat capacity, i.e., the inverse of the temperature rise per unit of supplied energy, evolving from a small to a high value around the relaxation time. In the case of a non-uniform light pattern, such as a Gaussian laser beam, the heat in the illuminated area finally diffuses to colder zones, resulting in a decrease in temperature. Finally, the temperature variation decreases to zero in the probed laser beam center.

For the simulations in Fig. 2, we have assumed the characteristic relaxation frequency ω_C to follow Vogel–Fulcher–Tammann (VFT) behavior,[47]

$$\omega_C = \omega_{C,0} \exp\left(-\frac{B}{T - T_{VFT}}\right), \tag{13}$$

where $\omega_{C,0}$ (s^{-1}) is a constant, T (K) is the temperature, and B (K) and T_{VFT} (K) are VFT parameters. The lower the DC temperature, the longer it takes for the temperature to decrease, i.e., for the effective instantaneous heat capacity to evolve from its instantaneous

TABLE I. Thermal parameters of glycerol, as determined from the literature,[30,48] used for the simulations in Fig. 2.

Quantity and symbol	Values	Unit
High-frequency limit of specific heat capacity (C_∞)	1180	J kg^{-1} K^{-1}
Low-frequency limit of specific heat capacity (C_0)	2100	J kg^{-1} K^{-1}
Relaxation frequency of specific heat capacity ($\omega_{C,0}$)	$5.75 \cdot 10^{14}$	s^{-1}
B	2210	K
T_{VFT}	133	K
Thermal conductivity (κ)	0.29	W m^{-1} K^{-1}
Density (ρ)	1260	Kg m^{-3}
Peak position of the laser pulse (t_0)	10	ns
Full width at half maximum of laser pulse ($FWHM$)	10	ns

Published under an exclusive license by AIP Publishing

value C_∞ to its long term limit C_0. In other words, the channeling of vibrational energy to the configurational network rearrangement (volume increasing) would occur around τ_C, which is the reciprocal of the relaxation frequency in Eq. (13) . At 200 K, the onset of this relaxation process is preceded by the thermal diffusion-driven wash out of the photothermally deposited heat and temperature gradient.

B. Photothermally induced displacement and strain response in a relaxing system

In this part, we focus on the relaxation behavior of thermoelastic transients triggered by the nonuniform temperature variation. To this end, we combine Newton's equation with the stress–strain relation for an anisotropic material (Hooke's law). In cylindrical coordinates (r, θ), this yields[49,50]

$$\begin{cases} \rho\dfrac{\partial^2 u_r}{\partial t^2} = \dfrac{1}{r}\dfrac{\partial}{\partial r}(r\sigma_{rr}) + \dfrac{1}{r}\dfrac{\partial \sigma_{r\theta}}{\partial \theta} - \dfrac{\sigma_{\theta\theta}}{r} - (3\lambda+2\mu)\gamma\dfrac{\partial T}{\partial r}, \\ \rho\dfrac{\partial^2 u_\theta}{\partial \theta^2} = \dfrac{1}{r^2}\dfrac{\partial}{\partial r}\left(r^2\sigma_{r\theta}\right) + \dfrac{1}{r}\dfrac{\partial \sigma_{\theta\theta}}{\partial \theta} - (3\lambda+2\mu)\gamma\dfrac{\partial T}{\partial \theta} \end{cases} \tag{14}$$

with

$$\begin{cases} \sigma_{rr} = (\lambda+2\mu)\dfrac{\partial u_r}{\partial r} + \dfrac{\lambda}{r}\dfrac{\partial u_\theta}{\partial \theta} + \dfrac{\lambda}{r}u_r, \\ \sigma_{\theta\theta} = \lambda\dfrac{\partial u_r}{\partial r} + (\lambda+2\mu)\dfrac{1}{r}\dfrac{\partial u_\theta}{\partial \theta} + (\lambda+2\mu)\dfrac{u_r}{r}, \\ \sigma_{r\theta} = \dfrac{\mu}{r}\dfrac{\partial u_r}{\partial \theta} + \mu\dfrac{\partial u_\theta}{\partial r} - \dfrac{\mu}{r}u_\theta, \end{cases} \tag{15}$$

where u_r (m) and u_θ (m) are the displacements in r and θ directions, respectively; λ (Pa) and μ (Pa) are the rigidity and shear modulus, respectively; σ_{rr} (Pa), $\sigma_{\theta\theta}$ (Pa), and $\sigma_{r\theta}$ (Pa) represent the stress components; and γ (K^{-1}) is the linear expansion coefficient. In our case, due to symmetry consideration, the displacement component in the θ direction vanishes. Thus, inserting Eq. (15) into Eq. (14), we obtain for $u_r \equiv u(r, t)$

$$\frac{\partial^2 u}{\partial r^2} + \frac{1}{r}\frac{\partial u}{\partial r} - \frac{u}{r^2} - \frac{\rho}{\lambda+2\mu}\frac{\partial^2 u}{\partial t^2} = \frac{3\lambda+2\mu}{\lambda+2\mu}\gamma\frac{\partial \Delta T}{\partial r}. \tag{16}$$

Fourier transforming Eq. (16) yields for $\tilde{u}(r, \omega)$

$$\frac{\partial^2 \tilde{u}}{\partial r^2} + \frac{1}{r}\frac{\partial \tilde{u}}{\partial r} - \frac{\tilde{u}}{r^2} + \frac{\rho\omega^2}{\lambda+2\mu}\tilde{u} = \frac{3\lambda+2\mu}{\lambda+2\mu}\gamma\frac{\partial \Delta \tilde{T}}{\partial r}. \tag{17}$$

Similarly, $\tilde{u}$ can also be expanded in terms of a Fourier Bessel series as follows:

$$\tilde{u}(r, \omega) = \sum_{m=1}^{\infty} J_1(q_m r)\varphi_m(\omega), \tag{18}$$

where $q_m = j_{0m}/R$, j_{1m} is the mth root of the first-order Bessel function $J_1(x)$, and $\varphi_m(\omega)$ is the corresponding Fourier Bessel coefficients. Inserting Eq. (18) into Eq. (17) and using the orthogonality properties of the Bessel function (see supplementary material C for a detailed calculation), the unknown Fourier Bessel coefficient $\varphi_m(\omega)$ can be solved as

$$\varphi_m(\omega) = \frac{2}{R^2 J_2^2(j_{1m})}\frac{\gamma(3\lambda+2\mu)/\rho}{\omega^2 - q_m^2(\lambda+2\mu)/\rho}\int_0^R \frac{\partial \tilde{T}}{\partial r}J_1(q_m r)rdr. \tag{19}$$

From Eq. (9), we have

$$\frac{\partial \Delta \tilde{T}}{\partial r} = \sum_{n=1}^{\infty} J_1(q_n r)\frac{Q_0 I_n q_n}{\pi\rho C_\infty J_1^2(j_{0n})R^2} \times \frac{i(\omega - i\omega_C)}{(\omega-\omega_{1n})(\omega-\omega_{2n})}. \tag{20}$$

By defining $F_{mn}(q_m, q_n) = \int_0^R J_1(q_n r)J_1(q_m r)rdr$, the displacement vector in the frequency domain can be written as

$$\tilde{u}(r, \omega) = \sum_{m=1}^{\infty}\sum_{n=1}^{\infty}\left(\begin{array}{l} J_1(q_m r)\dfrac{2iQ_0 I_n q_n}{\pi\rho C_\infty R^4 J_1^2(j_{0n})J_2^2(j_{1m})}F_{mn}(q_m, q_n) \\ \times\dfrac{(\omega - i\omega_C)}{(\omega-\omega_{1n})(\omega-\omega_{2n})} \times \dfrac{\gamma(3\lambda+2\mu)/\rho}{\omega^2 - q_m^2(\lambda+2\mu)/\rho} \end{array}\right), \tag{21}$$

where $\lambda + 2\mu$ is called the longitudinal modulus (M). M/ρ is equal to the square of the complex longitudinal velocity c_L (m s^{-1}), and μ/ρ is equal to the square of the shear velocity c_T (m s^{-1}). Thus, Eq. (21) can be rewritten as

$$\tilde{u}(r, \omega) = \sum_{m=1}^{\infty}\sum_{n=1}^{\infty}\left(\begin{array}{l} J_1(q_m r)\dfrac{2iQ_0 I_n q_n}{\pi\rho C_\infty R^4 J_1^2(j_{0n})J_2^2(j_{1m})}F_{mn}(q_m, q_n) \\ \times\dfrac{(\omega - i\omega_C)}{(\omega-\omega_{1n})(\omega-\omega_{2n})} \times \dfrac{\gamma\left(3c_L^2 - 4c_T^2\right)}{\omega^2 - q_m^2 c_L^2} \end{array}\right). \tag{22}$$

The linear thermal expansion coefficient, longitudinal bulk wave velocity, and shear wave velocity are all relaxing physical quantities.[33,51,52] To a reasonable approximation, these can be described by the Debye model as follows:

$$\begin{aligned} \gamma(\omega) &= \gamma_\infty + \frac{\Delta\gamma}{1 + i\omega/\omega_\gamma}, \\ c_L &= c_{L,\infty} + \frac{\Delta c_L}{1 + i\omega/\omega_{c_L}}, \\ c_T &= c_{T,\infty} + \frac{\Delta c_T}{1 + i\omega/\omega_{c_T}}, \end{aligned} \tag{23}$$

where $\Delta\gamma = \gamma_0 - \gamma_\infty$; $\Delta c_L = c_{L,0} - c_{L,\infty}$; $\Delta c_T = c_{T,0} - c_{T,\infty}$; γ_0, $c_{L,0}$, and $c_{T,0}$ and γ_∞, $c_{L,\infty}$, and $c_{T,\infty}$ are the low-frequency and high-frequency limits of the thermal expansion coefficients, longitudinal bulk wave velocity, and shear wave velocity, respectively. ω_γ, ω_{cL}, and ω_{cT} are characteristic (angular) frequencies, which are temperature dependent. Upon the substitution of Eq. (23) into Eq. (22) and assuming $\omega_{cL} = \omega_{cT}$, we find for $\tilde{u}(r, \omega)$

$$\tilde{u}(r, \omega) = \sum_{m=1}^{\infty}\sum_{n=1}^{\infty}\left(\begin{array}{l} J_1(q_m r)\dfrac{2iQ_0 I_n q_n \gamma_\infty\left(3c_{L,\infty}^2 - 4c_{T,\infty}^2\right)}{\pi\rho C_\infty R^4 J_1^2(j_{0n})J_2^2(j_{1m})}F_{mn}(q_m, q_n) \\ \times\dfrac{(\omega-\omega_8)(\omega-\omega_9)(\omega-\omega_{10})(\omega-\omega_{11})}{(\omega-\omega_{1n})(\omega-\omega_{2n})(\omega-\omega_3)(\omega-\omega_{4m})(\omega-\omega_{5m})(\omega-\omega_{6m})(\omega-\omega_{7m})} \end{array}\right) \tag{24}$$

Published under an exclusive license by AIP Publishing

with

$$\omega_3 = i\omega_\gamma,$$
$$\omega_{4m} = \frac{1}{2}\left(-q_m c_{L,\infty} + i\omega_{c_L} - \sqrt{(q_m c_{L,\infty} - i\omega_{c_L})^2 + 4iq_m\omega_{c_L}c_{L,0}}\right),$$
$$\omega_{5m} = \frac{1}{2}\left(-q_m c_{L,\infty} + i\omega_{c_L} + \sqrt{(q_m c_{L,\infty} - i\omega_{c_L})^2 + 4iq_m\omega_{c_L}c_{L,0}}\right),$$
$$\omega_{6m} = \frac{1}{2}\left(q_m c_{L,\infty} + i\omega_{c_L} - \sqrt{(q_m c_{L,\infty} + i\omega_{c_L})^2 - 4iq_m\omega_{c_L}c_{L,0}}\right),$$
$$\omega_{7m} = \frac{1}{2}\left(q_m c_{L,\infty} + i\omega_{c_L} + \sqrt{(q_m c_{L,\infty} + i\omega_{c_L})^2 - 4iq_m\omega_{c_L}c_{L,0}}\right), \quad (25)$$
$$\omega_8 = i\omega_C,$$
$$\omega_9 = i\omega_\gamma/\left(1 - \frac{\Delta\gamma}{\gamma_0}\right),$$
$$\omega_{10} = i\omega_{c_L}\frac{\sqrt{3}c_{L,0} + 2c_{T,0}}{\sqrt{3}c_{L,\infty} + 2c_{T,\infty}},$$
$$\omega_{11} = i\omega_{c_L}\frac{\sqrt{3}c_{L,0} - 2c_{T,0}}{\sqrt{3}c_{L,\infty} - 2c_{T,\infty}}.$$

Since for all q_m values, $\mathrm{Im}(\omega_3) > 0$, $\mathrm{Im}(\omega_{4m}) > 0$, $\mathrm{Im}(\omega_{5m}) > 0$, $\mathrm{Im}(\omega_{6m}) > 0$, and $\mathrm{Im}(\omega_{7m}) > 0$, $\tilde{u}(r,\omega)$ gains five additional singularities at $\omega = \omega_3$, $\omega = \omega_{4m}$, $\omega = \omega_{5m}$, $\omega = \omega_{6m}$, and $\omega = \omega_{7m}$ (see supplementary material B). Similar to Sec. II A, by applying the residue theorem, we transform Eq. (24) back to time domain,

$$u(r,t) = -\sum_{m=1}^{\infty}\sum_{n=1}^{\infty}\left(\begin{array}{l} J_1(q_m r)\dfrac{4Q_0 I_n q_n \gamma_\infty\left(3c_{L,\infty}^2 - 4c_{T,\infty}^2\right)}{\rho C_\infty R^4 J_1^2(j_{0n})J_2^2(j_{1m})} \\ \times F_{mn}(q_m,q_n)\left(\sum_{i=1}^{2} A_{in}\exp(i\omega_{in}t)\right. \\ \left. + A_3\exp(i\omega_3 t) + \sum_{j=4}^{7} A_{im}\exp(i\omega_{im}t)\right)\end{array}\right)H(t), \quad (26)$$

with

$$\begin{cases} A_{1n} = \dfrac{(\omega_{1n}-\omega_8)(\omega_{1n}-\omega_9)(\omega_{1n}-\omega_{10})(\omega_{1n}-\omega_{11})}{(\omega_{1n}-\omega_{2n})(\omega_{1n}-\omega_3)\prod_{i=4}^{7}(\omega_{1n}-\omega_{im})}, \\ A_{2n} = \dfrac{(\omega_{2n}-\omega_8)(\omega_{2n}-\omega_9)(\omega_{2n}-\omega_{10})(\omega_{2n}-\omega_{11})}{(\omega_{2n}-\omega_{1n})(\omega_{2n}-\omega_3)\prod_{i=4}^{7}(\omega_{2n}-\omega_{im})}, \\ A_3 = \dfrac{(\omega_3-\omega_8)(\omega_3-\omega_9)(\omega_3-\omega_{10})(\omega_3-\omega_{11})}{(\omega_3-\omega_{1n})(\omega_3-\omega_{2n})\prod_{i=4}^{7}(\omega_3-\omega_{im})}, \\ A_{4m} = \dfrac{(\omega_{4m}-\omega_8)(\omega_{4m}-\omega_9)(\omega_{4m}-\omega_{10})(\omega_{4m}-\omega_{11})}{(\omega_{4m}-\omega_{1n})(\omega_{4m}-\omega_{2n})(\omega_{4m}-\omega_3)\prod_{i=5}^{7}(\omega_{4m}-\omega_{im})}, \\ A_{5m} = \dfrac{(\omega_{5m}-\omega_8)(\omega_{5m}-\omega_9)(\omega_{5m}-\omega_{10})(\omega_{5m}-\omega_{11})}{(\omega_{5m}-\omega_{1n})(\omega_{5m}-\omega_{2n})(\omega_{5m}-\omega_3)\prod_{i=4\neq5}^{7}(\omega_{5m}-\omega_{im})}, \\ A_{6m} = \dfrac{(\omega_{6m}-\omega_8)(\omega_{6m}-\omega_9)(\omega_{6m}-\omega_{10})(\omega_{6m}-\omega_{11})}{(\omega_{6m}-\omega_{1n})(\omega_{6m}-\omega_{2n})(\omega_{6m}-\omega_3)\prod_{i=4\neq6}^{7}(\omega_{6m}-\omega_{im})}, \\ A_{7m} = \dfrac{(\omega_{7m}-\omega_8)(\omega_{7m}-\omega_9)(\omega_{7m}-\omega_{10})(\omega_{7m}-\omega_{11})}{(\omega_{7m}-\omega_{1n})(\omega_{7m}-\omega_{2n})(\omega_{7m}-\omega_3)\prod_{i=4}^{6}(\omega_{7m}-\omega_{im})}. \end{cases} \quad (27)$$

The refractive index variations that are responsible for the thermal lens signal are essentially proportional to the radial density or strain variations resulting from the varying temperature and pressure fields, which are given as

$$\varepsilon(r,t) = -\frac{\partial u(r,t)}{\partial r} = \sum_{m=1}^{\infty}\sum_{n=1}^{\infty}\left(\begin{array}{l} (J_0(q_m r) - J_2(q_m r)) \\ \times \dfrac{2Q_0 I_n q_m q_n \gamma_\infty\left(3c_{L,\infty}^2 - 4c_{T,\infty}^2\right)}{\rho C_\infty R^4 J_1^2(j_{0n})J_2^2(j_{1m})} \\ \times F_{mn}(q_m,q_n)\left(\sum_{i=1}^{2} A_{in}\exp(i\omega_{in}t)\right. \\ \left. + A_3\exp(i\omega_3 t) + \sum_{i=4}^{7} A_{im}\exp(i\omega_{im}t)\right)\end{array}\right)H(t). \quad (28)$$

The first term of Eq. (28) contains the thermal damping parameters ω_{1n} and ω_{2n}, which are related to the thermal diffusion constant $q_n^2\alpha_0$ and the relaxation parameters of specific heat capacity. The second term (i.e., ω_3) represents the thermal expansion relaxation with relaxation time $1/\omega_\gamma$. The angular frequencies ω_{4m}, ω_{5m}, ω_{6m}, and ω_{7m} in the last term are related to the longitudinal bulk wave velocity and absorption coefficient, so the last term governs the contributions of acoustic waves to the strain response. The infinite sums over n and m indices in Eq. (28) can be truncated to $n = \overline{N}$ and m = $\overline{N}$. It was found that $\overline{N} = 500$ provides a good approximation to the infinite sum. The higher values of $\overline{N}$ substantially do not vary the result.

Figure 3 illustrates the normalized strain response to photothermal heating at a radius of ~30 μm and a duration pump beam laser pulse of ~10 ns, which is Gaussian in space and in time, in the x–y plane in the axial focus of the pump beam ($z = z_1$) at different times. Clear radial patterns in the strain, and thus in the refractive index, the radial gradient of which evokes a (thermal and acoustic) lens effect for the trespassing probe beam, can be observed upon the absorption of the laser pulse. Shortly after the deposition of the optical energy [between 0 and 15 ns, Figs. 3(a)–3(c)], due to the impulsiveness and localized character of the thermal expansion, a pressure wave radially leaves the excitation region, with a speed of about 70 μm per 25 ns. Interestingly, for the simulated temperature, the configurational part of the thermal expansion, which is substantially larger than the initial, short time limit of the thermal expansion, occurs only after about 10 μs, i.e., the respective relaxation time, explaining the maximum strain in Fig. 3(e). The following decay is related to the thermal diffusion-driven wash out of the hotspot and thus of the strain gradient. The simulation also shows that the thermal part of the strain pattern is characterized by a central peak, with a radially monotonically decaying pattern, somewhat comparable with a regular diverging lens. However, the acoustic wave induced strain pattern has a ring shape, for which a non-trivial lens effect can be expected.

Accompanied by the local and transient thermal expansion, acoustic waves will also contribute to the TL signals on a short time scale [(b) and (c)], determined by the probe beam size and the group sound velocity. Thus, the TL effect can be considered as the superposition of the temperature lens and the acoustic lens, thereby altering the propagating probe wavefront. Tables II and III summarize all the involved parameters for simulating Fig. 3.

Published under an exclusive license by AIP Publishing

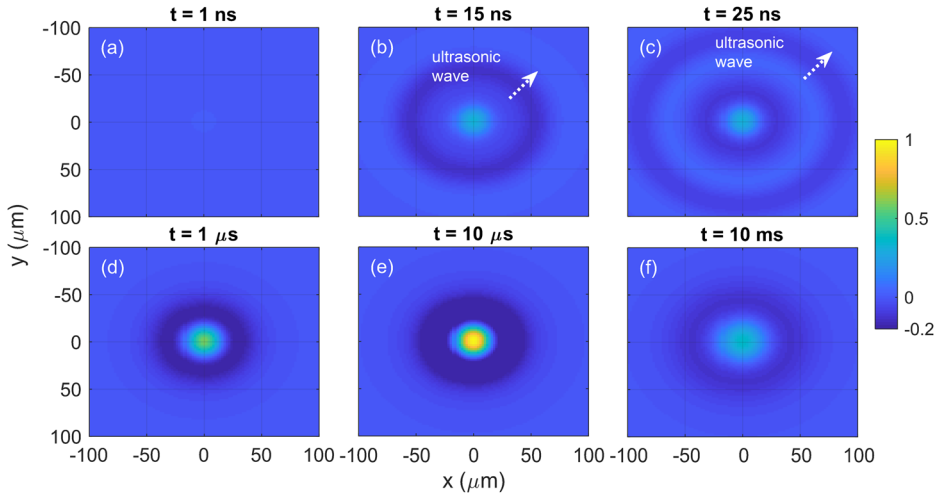


FIG. 3. Simulated evolution of the normalized radial strain response of glycerol at 230 K at the beam center (z1) at different times: (a) t = 1 ns, (b) t = 10 ns, (c) t = 30 ns, (d) t = 1 μs, (e) t = 10 μs, and (f) t = 10 ms (Multimedia view). The depicted x–y plane is perpendicular to the pump laser beam axis. The laser-induced acoustic pulses (ring), marked with white arrows, travel about 70 μm in 25 ns. Parameters in Tables II and III were used for the simulation. Movies of the full trajectories are available in the supplementary material.

TABLE II. Thermoelastic parameters of glycerol, determined from the literature,[51,53,54] used in the simulation of Fig. 3.

Quantity and symbol	Values	Unit
High-frequency limit of thermal expansion (γ_∞)	10^{-4}	K^{-1}
Low-frequency limit of thermal expansion (γ_0)	$6 \cdot 10^{-4}$	K^{-1}
Relaxation frequency of thermal expansion (ω_γ)	$1.96 \cdot 10^5$	s^{-1}
Low-frequency limit of longitudinal wave velocity ($c_{L,0}$)	2050	m s^{-1}
High-frequency limit of longitudinal wave velocity ($c_{L,\infty}$)	3370	m s^{-1}
Relaxation frequency of longitudinal wave velocity (ω_{cL})	$2.38 \cdot 10^5$	s^{-1}
Low-frequency limit of shear wave velocity ($c_{T,0}$)	0	m s^{-1}
High-frequency limit of shear wave velocity ($c_{T,\infty}$)	1400	m s^{-1}

C. TL signals

The TL detection is typically performed by analyzing the on-axis intensity variation of the central part of the probe beam in the far-field, where the photodetector is located. The TL effect is based on the radially non-uniform optical phase delay that acts on the light beam propagation in the same way as a lens. The phase shift can be expressed as

$$\begin{aligned}\Delta\psi(r,t) &= k_p \Delta n L \\ &= k_p n \chi \varepsilon(r,t) L,\end{aligned} \tag{29}$$

where $k_p = 2\pi/\lambda_p$ (m^{-1}) is the wavenumber, with λ_p (nm) the wavelength of the probe beam; L (mm) is the thickness of the sample; and χ is the scale factor, which is a constant. The TL formed in the sample has a transmission function defined as $\exp(-i\Delta\psi(r,t))$. Thus, the TEM00 Gaussian probe beam in the proximity of the sample can be expressed as[43]

$$\begin{aligned}U_p(r,z_1,t) = &\sqrt{\frac{2P_p}{\pi}}\frac{1}{\omega_{1p}}\exp(-ik_p z_1) \\ &\times \exp\left[-i\left(\frac{k_p r^2}{2R_{1p}} + \Delta\psi(r,t)\right) - \frac{r^2}{\omega_{1p}^2}\right],\end{aligned} \tag{30}$$

where P_p (W) is the total probe beam power and R_{1p} (m) is the radius of curvature of the probe beam wavefronts at z_1. The probe beam propagating out of the sample to the detector plane can be obtained by applying Fresnel diffraction theory[55,56] to Eq. (30). As only the center point of the probe beam, which passes through the pinhole, is detected in our experiment, using cylindrical coordinates, Fresnel integration gives[43]

$$U_p(z_1+z_2,t) = \frac{ik_p}{z_2}\exp(-ik_p z_2)\int_0^\infty U_p(r,z_1,t)\exp\left(-i\frac{k_p r^2}{2z_2}\right)rdr. \tag{31}$$

TABLE III. Experimental parameters of the beam configuration for the geometry shown in Fig. 1.

Quantity and symbol	Values	Unit
Pump laser radius at the sample (ω_e)	30	μm
Probe laser waist radius (ω_{0p})	100	μm
Thickness of the sample cell (L)	2	mm
Distance z_2	1.5	m

For the Gaussian probe beam,[43]

$$\begin{aligned}\omega_{1p}^2 &= \omega_{0p}^2\left[1 + (z_1/z_R)^2\right], \\ R_{1p} &= \left(z_1^2 + z_R^2\right)/z_1,\end{aligned} \tag{32}$$

Published under an exclusive license by AIP Publishing

where $z_R = \pi\omega_{0p}^2/\lambda_p$. Thus, by inserting Eq. (30) into Eq. (31), we can get

$$U_p(z_1+z_2,t) = A\int_0^\infty \exp(-i\Delta\psi(r,t))\exp\left(-(iV+1)\frac{r^2}{\omega_{1p}^2}\right)rdr, \tag{33}$$

where $A = \frac{ik_p}{z_2\omega_{1p}}\sqrt{\frac{2P_p}{\pi}}\exp(-ik_p(z_1+z_2))$ and $V = \frac{z_1}{z_R} + \frac{z_R}{z_2}\left(1+\frac{z_1^2}{z_R^2}\right)$. Due to the low optical absorption of the sample, the phase shift is very small [$\Delta\psi\ (r,\ t) \ll 1$]. Thus, an approximation can be made, $\exp(-i\Delta\psi\ (r,\ t)) \approx 1 - i\Delta\psi\ (r,\ t)$.[39] Substituting Eqs. (28) and (29) into Eq. (33), we can get

$$\begin{aligned} U_p(z_1+z_2,t) &\approx A\int_0^\infty (1-i\Delta\psi(r,t))\exp\left(-(iV+1)\frac{r^2}{\omega_{1p}^2}\right)rdr \\ &= A\left\{\frac{\omega_{1p}^2}{2(1+iV)} - \sum_{m=1}^{\infty}\sum_{n=1}^{\infty}\left(\frac{2iQ_0I_nq_mq_n\gamma_\infty k_p n\chi L\left(3c_{L,\infty}^2 - 4c_{T,\infty}^2\right)}{\rho C_\infty R^4 J_1^2(j_{0n})J_2^2(j_{1m})}F_{mn}(q_m,q_n)\right.\right. \\ &\quad \left.\left.\times\left(\sum_{i=1}^{2}A_{in}\exp(i\omega_{in}t) + A_3\exp(i\omega_3 t) + \sum_{i=4}^{7}A_{im}\exp(i\omega_{im}t)\right)\right)(F_0(q_m) - F_2(q_m))\right\}H(t), \end{aligned} \tag{34}$$

with

$$\begin{cases} F_0(q_m) = \int_0^\infty \exp\left(-(iV+1)\frac{r^2}{\omega_{1p}^2}\right)J_0(q_m r)rdr, \\ F_2(q_m) = \int_0^\infty \exp\left(-(iV+1)\frac{r^2}{\omega_{1p}^2}\right)J_2(q_m r)rdr, \end{cases} \tag{35}$$

where $F_0(q_m)$ and $F_2(q_m)$ are the zero-order and second-order Hankel transforms of $\exp\left(-(iV+1)\frac{r^2}{\omega_{1p}^2}\right)$, respectively. The final probe beam intensity (W m^{-2}) at the center of the detector plane can be expressed as

$$I(z_1+z_2,t) = \frac{c\varepsilon_0}{2}|U_p(z_1+z_2,t)|^2, \tag{36}$$

where c (m s^{-1}) is the speed of light and ε_0 (F m^{-1}) is the permittivity of free space.

III. EXPERIMENTAL TL SPECTROSCOPY OF GLASSY DYNAMICS

A. Experimental setup

Heretofore, we have presented the modeling of the TL transients in relaxing systems. We now illustrate an experimental investigation of the glassy dynamics in supercooled glycerol, a well-characterized molecular glass former,[57–60] using time-resolved TL spectroscopy and the model developed above. Figure 4 depicts the experimental setup. A pulsed ND: YAG laser (Model Lab-130-10, Quanta-Ray®) operating at 1064 nm with a pulse width of 10 ns was used to excite the glycerol sample (>99% purity). The excitation laser was focused inside the sample using a focal length lens (L) of 125 mm. A continuous 532-nm TEM00 probe laser (Model Samba 100, Cobolt®), inserted through a dichroic mirror coaxially with an excitation laser and focused by the same lens, was used to probe the global strain response to impulsive heating. The sample was sealed in a cuvette [optical path: 2 mm, 45 mm (H) × 12 mm (L) × 12 mm (W)] and attached to the cold finger of an optical cryostat (Model Optistat-DN-V, Oxford Instruments®), allowing DC temperature control and/or scan over the sample.

In this experiment, the focal waist of the probe laser (green) and pump laser (red) is displaced with respect to each other inside the sample due to the aberration of the focusing lens,[61] yielding the so-called mode-mismatched configuration[43] (see the geometry in Fig. 1). After passing through the sample, the intensity of the probe beam was detected using a homemade photodetector (PD, bandwidth: ~100 MHz) in the far-field. A pinhole with a diameter of 1 mm was placed in front of the detector to enhance the detection of TL signals. Furthermore, an interference filter (IF) was placed in front of the pinhole to block the transmitted excitation light. The output of the PD was coupled to a fast oscilloscope (LC564A, Lecroy®). In our experiment, the excitation laser repetition rate was 10 Hz, and 500 TL cycles were recorded and averaged using the oscilloscope to reduce the noise. Table III summarizes the experimental parameters of optics.

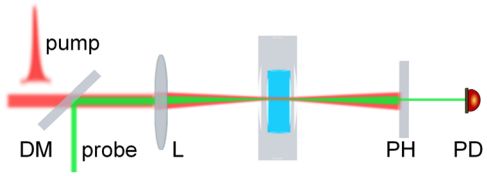


FIG. 4. Experimental setup of *ns* TL spectroscopy: DM, dichroic mirror; L, lens; PH, pinhole; and PD, photodetector.

Published under an exclusive license by AIP Publishing

B. Results and discussion

We recorded TL waveforms in a time window of about 20 ms at 12 selected temperatures from 300 to 200 K. Figure 5 summarizes all the waveforms (symbols) and the best fits (solid lines) with the model developed in this work, namely, via Eq. (36). Three subsequent processes can be observed: (1) a rapid increase in amplitude (0.5–80 ns), corresponding to the fast part of the temperature rise and the resulting thermal expansion response to the sudden heat input; (2) a slow rise due to the slow part of the thermal expansion and underlying temperature dynamic time span; (3) an exponential thermal dissipation back to zero, with a characteristic thermal diffusion decay time determined by the width of the pump laser beam at the focal point. With decreasing DC temperature, the process (3) occurs at later times until it is quenched by the thermal diffusion decay of the signal. With increasing DC temperature, it occurs at earlier times until it overlaps with the initial, fast part of the thermal expansion. On a longer time scale, because more energy flows to evoke cooperative rearrangements of the amorphous network, the heat capacity increases toward C_0, dominating the thermal diffusion part. It is worth to mention that, in a TL scheme, the measured global strain response to impulsive heating can be considered as a convolution between the temperature response to impulsive heating (with the specific heat as the response parameter) and the strain response to a sudden temperature rise (with the thermal expansion coefficient as the response parameter). Due to its time-varying and often spatially non-uniform character, the local thermal expansion response is unavoidably accompanied by the launching of acoustic waves, which carry information on the (relaxation behavior of the) elastic modulus.

In addition, in many respects, the pulsed TL scheme is similar to that of the transient grating (TG) or impulsive stimulated thermal scattering (ISTS).[48,62] The main difference between the two approaches lies in the geometry of the optical excitation pattern: while in TG, the light pattern is spatially periodic and characterized by a single wavenumber, the Gaussian pattern used in a TL configuration results in a wide spectrum in the wavenumber domain. This difference in the spectral content has consequences mainly concerning the following: (1) the thermal diffusion tail, which is purely exponential for TG signals and more complicated for TL signals, and (2) the initial acoustic signals, which are a set of damped sinusoid oscillations for TG signals and a bipolar acoustic pulse in TL signals. Interesting to mention is also the modeling of the ISTS response, in which the relaxation of heat capacity and thermal expansion are not envisaged as two separate processes. Instead, this combined effect of temperature change and thermal expansion has been modeled by making use *ad hoc* of a single stretched exponential function, $e^{(-t/f_R)^{\beta}}$, with f_R the structural relaxation frequency and β the stretching exponent (<1). Given indications that the two relaxing quantities may indeed be characterized by different time scales[19] at least for some glass formers and given an increasing interest in the field of glass transition research in comparing the time scale of different relaxation quantities,[36,63] in this work, we have tackled the challenge to model the density response that explicitly treats the two as independent relaxation quantities. An apparent benefit is that it

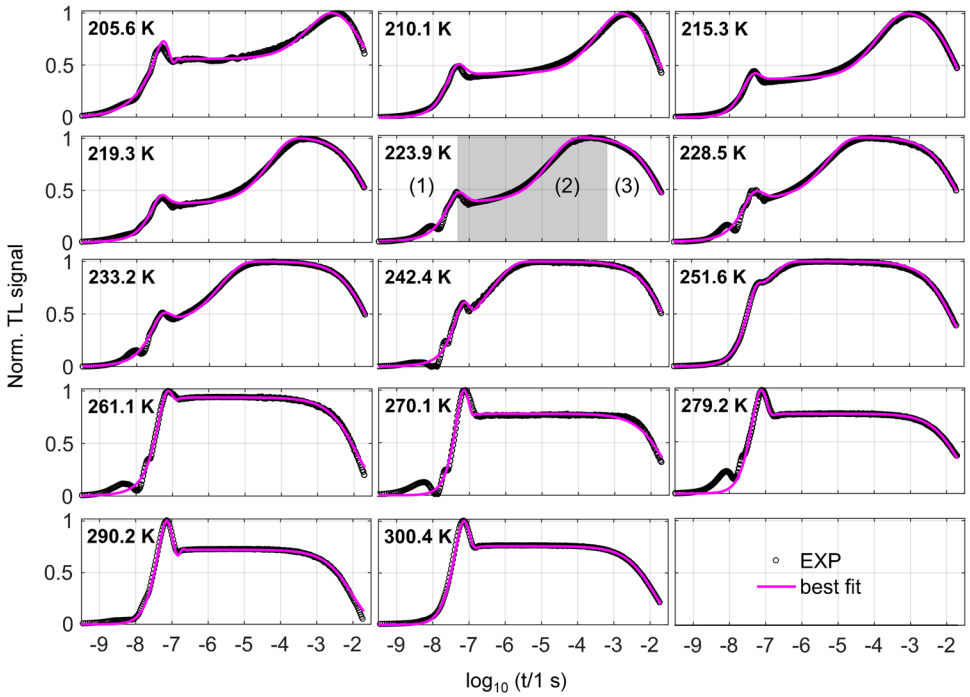


FIG. 5. Normalized TL signals of glycerol at a selection of temperatures (symbol, black) and best fits (solid line, magenta) via Eq. (36). A strongly (DC) temperature-dependent double-step-like strain response can be observed at intermediate times [area (2)]. The discrepancy between experimental data and best fits is mainly found at the very short time scale, namely, fitting of the acoustic part, which will be discussed in the Appendix.

Published under an exclusive license by AIP Publishing

makes it possible to simultaneously assess the relaxation of C(ω) and $\gamma(\omega)$.

Figure 5 shows that satisfactory fitting quality has overall been achieved at all temperatures, suggesting that the model developed in this work can describe well the experimental data. To take into account the possible covariance of the involved multiple fitting variables, we have implemented a most squares error (MSE) analysis[64] to determine the fitting uncertainty, as shown in Fig. 6. For each fitting parameter, the MSE analysis is performed by evaluating the cost function, which is defined as the sum of the squared residuals (SSR) corresponding to the time vector t [Eq. (37)] over a broad range centered around the best-fitting values, P_0, without fixing the other fitting parameters. On the contrary, in a least-squares error (LSE) analysis, the rest fitting parameters are fixed at their best-fitting values, and only the parameter to be evaluated is varied in a region around its best-fitting value,

$$\chi^2 = \frac{1}{N}\sum_{i=1}^{N}\left(TL_{\exp}(t_i) - TL_{fit}(t_i, P_0)\right)^2. \quad (37)$$

As an example, Fig. 6 illustrates the MSE (circles) and LSE (squares) evaluation of the four best-fit parameters for the fitting of the TL waveforms at 233.2 K. Each curve shows a parabolic behavior of the SSR around the best-fitting value, suggesting good convergence of the fitting/minimization procedure. The opening of the MSE curve is generally wider than that of the LSE curve since the former takes into account the covariance of the involved multiple fitting variables, namely, different combinations of fitting parameters, yielding a statistically indistinguishable cost function value (SSR). The finite width of the SSR parabola shows that the inverse problem of extracting the four fitting parameters from the TL signal is feasible. Hence, TL spectroscopy and the model developed in this work allow us to determine the thermal relaxation of specific heat capacity and thermal expansion coefficient. Here, we underline that in our modeling, we have approximated the relaxation with the Debye model, although the Havriliak–Negami (HN) relaxation model[65] has been shown to be reflecting better reality and although the HN model is more commonly used for the description of relaxation processes. We have chosen the Debye model mainly for the sake of feasibility to achieve an analytical solution, which is appealing. Interestingly, looking at the already very satisfactory fitting quality of our Debye-relaxation-based model to the experimental TL traces (Fig. 5), we can foresee that using the HN model would not improve considerably the fitting quality. Instead, it would increase significantly the complexity of model fitting (degeneracy) due to the involved four extra fitting parameters (covariance), which, in turn, would make it difficult to accurately extract the relaxation characteristics, with a reliable analysis of margins of uncertainty, as obtained in Fig. 6.

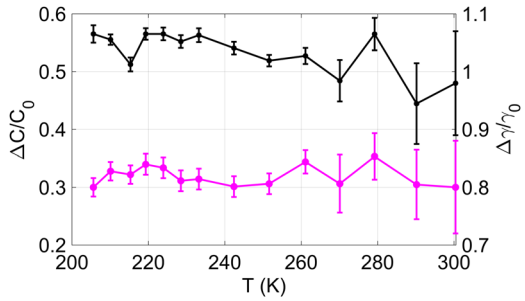


FIG. 7. The fitting values of $\Delta C/C_0$ (left, black) and $\Delta\gamma/\gamma_0$ (right, magenta) vs DC temperature. The error bar was obtained by most squares error analysis.

Figure 7 shows the fitted values of $\Delta C/C_0$ (left, black) and $\Delta\gamma/\gamma_0$ (right, magenta) at different temperatures. Within the uncertainty margin, no temperature dependence is observed. The average fitting value of $\Delta C/C_0$ and $\Delta\gamma/\gamma_0$, which is also termed the relaxation strength, is 0.53 ± 0.04 for specific heat capacity and 0.82 ± 0.02 for thermal expansivity. These values comply with literature values, 0.48 by 3-ω[26,27] and 0.44 by PPE[29,30] for specific heat capacity and 0.80 by DC dilatometry for expansivity.[53] C_0 is well defined in the thermal diffusion tail with the average fitting value of 2160 ± 200 J kg^{-1} K^{-1},

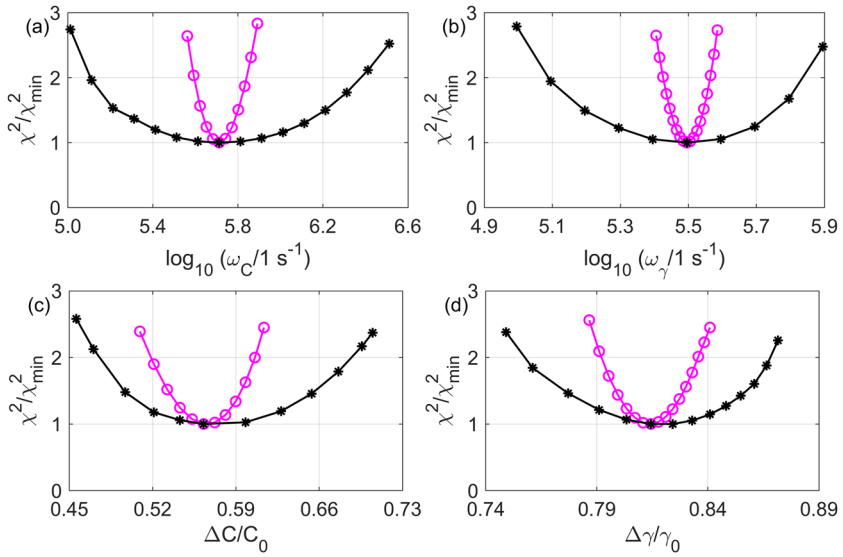


FIG. 6. Parabolic evolution of the least-squares (magenta circles) and most squares (black stars) cost function on the fitting parameters of (a) ω_C, (b) ω_γ, (c) $\Delta C/C_0$, and (d) $\Delta\gamma/\gamma_0$ for the TL signal at 233.2 K.

Published under an exclusive license by AIP Publishing

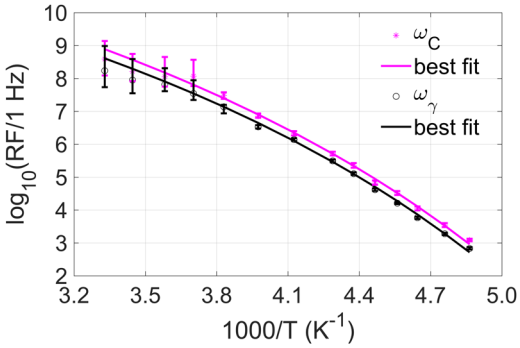


FIG. 8. VFT plot of the relaxation frequency (RF) of specific heat and thermal expansivity determined (symbols) and the best fit (solid line).

again in line with the literature values, 2100 by PPE and 2250 by 3-ω. We can then calculate C_∞ with the ratio shown in Fig. 7, yielding 1010 ± 90 J kg^{-1} K^{-1}, which agrees well with the results from PPE and 3-ω, 1180 and 1160, respectively. In our fitting, γ_∞ is fixed at 10^{-4} K^{-1},[53] and the average fitting value of γ_0 is 5.5 ± 0.6 10^{-4} K^{-1}.

Figure 8 shows the fitted relaxation frequency entering the specific heat capacity (ω_C) and thermal expansion (ω_γ) in the form of the Debye model. The fitting uncertainties (error bar) are also obtained by most squares analysis. Larger fitting uncertainties are found at high temperatures (>260 K) when the relaxation frequency approaches 100 MHz. This suggests that the finite linewidth of the pump laser pulse, around 10 ns, has limited access to higher frequencies, which can be extended by using shorter laser pulses, e.g., sourced from picosecond or femtosecond lasers. It should be underlined that the clear deviations in the VFT plot for 1000/T < 3.5 may be related to the so-called crossover temperature (285 K for glycerol[66]), where the faster Johari–Goldstein β relaxation tends to merge into the slower α relaxation.[67] The temperature dependence of relaxation frequency was fitted by the VFT equation (solid line) [Eq. (13)] with ω_0, B, and T_{VFT} as fitting parameters. Table IV summarizes the VFT parameters for the two relaxing quantities investigated in this work using the TL and their comparisons with the ones determined by other techniques, i.e., structural behavior by ISTS,[48] specific heat capacity by 3-ω[26,27] and PPE,[29,30] dielectric permittivity by broadband dielectric spectroscopy,[16] and compliance by heterodyne ultrasonic spectroscopy.[52] The fragility m is defined as[1]

$$m = \frac{d\,\log\langle\tau\rangle}{d(T_g/T)}\Big|_{T=T_g}, \tag{38}$$

with τ the relaxation time and T_g the glass transition temperature. Equation (38) an be approximated as[68]

$$m = 16 + \frac{590}{B/T_{VFT}}. \tag{39}$$

Table IV shows that the fragility values for the heat capacity and thermal expansion extracted from the TL experiments are consistent with the values in the literature, with each other, and with the fragility values of mechanical and rotational relaxation from ultrasonic and dielectric spectroscopy. This further confirms the earlier observations of the universality of relaxation features (fragility and shape features of the relaxation spectrum[19]) across different physical responses in the considered temperature range. From the values in Table IV, it can be extracted that for glycerol, the different relaxation frequencies vary within one decade, showing that in the considered temperature range, the respective processes are not decoupled. For a detailed discussion about time-scale decoupling, we refer to the study by Niss and Heckscher.[19] In an accompanying article,[62] we also show that, because of mathematical reasons, the relaxation time of a susceptibility probing a relaxation process can be quite different between the quantity and its inverse (e.g., elastic modulus and compressibility) and that this difference increases as the relative relaxation strength increases.

Table IV further shows that the relaxation strength of the thermal expansion coefficient and dielectric susceptibility[16] is substantially larger than that of the specific heat capacity and mechanical compliance.[52] This seems to reflect that thermally driven configurational volume changes related to molecular bond rotations are energetically less stringent than thermally driven volume changes due to increased anharmonic molecular vibrations. The relaxation strengths found using the TL technique, for both specific heat and thermal expansion, are somewhat different from those previously reported values by using other techniques. The discrepancy may also partially arise from the approximation of the Debye model in our modeling, whereas the HN model has been used in other techniques. One can numerically verify that for the same low and high-frequency limits of the real part of C(ω), the height of the relaxation peak in the imaginary part of C(ω) is substantially different between the Debye and HN models.

TABLE IV. Comparison of the VFT behavior and relaxation strength of glycerol probed by thermal, mechanical, and dielectric susceptibilities ($f_0 = \omega_0/2\pi$).

Relaxation dynamics	Measurement technique	$\log_{10}$ (f_0/1 Hz)	B (K)	T_{VFT} (K)	Fragility	Relaxation strength
Specific heat capacity	TL	13.40 ± 0.18	2220 ± 50	120 ± 2	47.8 ± 1.2	0.53 ± 0.04
Thermal expansivity	TL	13.00 ± 0.15	2160 ± 50	121 ± 2	49.1 ± 1.3	0.82 ± 0.02
Structure behavior[48]	ISTS	14.7	2210	133	51.5	0.66
Specific heat capacity[29,30]	PPE	11.9	1593	142	68.5	0.44
Specific heat capacity[27,28]	3-ω	14.6	2500	128	46.2	0.48
Compliance[52]	Ultrasonic spectroscopy	14.4	2310	129	48.9	0.60
Dielectric[16]	Dielectric spectroscopy	14.0	2309	129	49.0	0.92

Published under an exclusive license by AIP Publishing

IV. CONCLUSIONS AND OUTLOOK

In this paper, we have investigated the thermal relaxation dynamics in supercooled systems by making use of high bandwidth time-resolved thermal lens (TL) spectroscopy. We developed an analytical model to describe the time-resolved TL response in a relaxing system by taking into account the relaxation of specific heat (C) and thermal expansivity (γ). TL waveforms were experimentally acquired on supercooled glycerol in a broad time window, from 1 ns to 20 ms, in a wide temperature range, 200–300 K. The developed model was used to fit the experimental waveforms, allowing the evaluation of several key relaxation features of C and γ. The obtained low/high-frequency limit response, 2160 ± 200/1010 ± 90 J kg^{-1} K^{-1} for C and 10^{-4}/5.5 ± 0.6 10^{-4} K^{-1} for γ, and the respective relaxation strengths, 0.53 ± 0.04 and 0.82 ± 0.02, comply well with the ones determined by 3-ω,[26,27] PPE,[29,30] and DC dilatometry.[53] This confirms the reliability of the theoretical model and its adequate application to investigate glassy dynamics. The followed approach has allowed us to assess the slowing down process of the two processes involved in structural relaxation, i.e., the response of temperature and volume to heating. The obtained VFT behavior of the relaxation frequency in the sub-kHz to sub-100 MHz range largely extends the upper limit of the previously existing spectroscopy of C and γ, 100 kHz and 1 Hz, achieved by PPE and capacitive scanning dilatometry.[32,33] It should be mentioned that the bandwidth may be further extended by making use of shorter laser pulses. The obtained VFT plots of C and γ are found to be parallel in the probed temperature range. The respective fragilities are comparable to those of dielectric and mechanical susceptibilities, confirming the universal relaxation behavior between the different response functions. This work extends the application of TL spectroscopy to the determination of glassy dynamics. Although this work illustrated time-domain transient experiments based on pulsed-laser excitation, one could implement the concept in the frequency domain that involves CW excitation with a modulated intensity.

SUPPLEMENTARY MATERIAL

See the supplementary material for (1) the technical details of the derivation and (2) the movie of the full temporal evolution of the laser-induced TL effect in a relaxing system, illustrated in Fig. 3 (Multimedia view).

ACKNOWLEDGMENTS

C.G. and M.G. are grateful to the KU Leuven Research Council for financial support (Grant No. C14/16/063 OPTIPROBE). L.L. acknowledges the financial support from FWO (Research Foundation-Flanders) postdoctoral research fellowship (Grant Nos. 12V4419N and 12V4422N). P.Z. acknowledges the support of the Chinese Scholarship Council (CSC). M.G. acknowledges financial support from the National Research Council Joint Laboratories program [Project No. SAC.AD002.026 (OMEN)]. F.B. acknowledges financial support from the University de Lyon in the frame of the IDEXLYON Project (No. ANR-16-IDEX-0005) and University Claude Bernard Lyon 1 through the BQR Accueil EC 2019 grant.

APPENDIX: DETERMINATION OF ACOUSTIC RELAXATION

The main body of this work has focused on thermal relaxation dynamics, namely, $C(\omega)$ and $\gamma(\omega)$. The TL signals on the short time scale (<100 ns, Fig. 5) also contain acoustic signals, which are also undergoing substantial changes upon cooling due to the acoustic relaxation. The model developed in this work [Eq. (28)] took into account the Debye behavior [Eq. (23)] of the acoustic relaxation. In this Appendix, we discuss the possibility to extract the acoustic relaxation dynamics based on model fitting. This simply involves the longitudinal wave parameters as fitting variables only, as the contribution of the shear wave to the TL signal in our geometry is small. Figure 9 (left) shows the fitted values of $c_{L,0}$ (1740 ± 250 m/s) and $c_{L,\infty}$ (3350 ± 180 m/s), which are consistent with the results reported in Refs. 48 and 62 (about 1800 and 3600 m/s). Figure 9 (right) shows the obtained acoustic relaxation frequencies, from which we only see a very weak slowing down process upon cooling. This does not comply with results in the literature (Fig. 4 of Ref. 52) and neither reflects the physical process one would expect, i.e., a much stronger slowing down process similar to C and γ (Fig. 8). However, this discrepancy does not invalidate the modeling, as it is a consequence from the limited acoustic bandwidth/dynamic range in the TL, about 15–20 MHz, which does not cover the entire frequency scale that characterizes the acoustic relaxation in such a broad temperature range. This argumentation is further supported by the fitting quality of the acoustic signals: satisfactory fitting was only achieved at very high (>270 K) and low (<220 K) temperatures, where

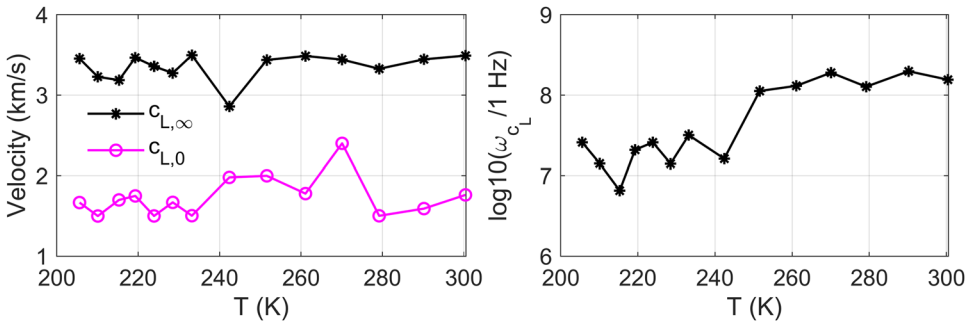


FIG. 9. Temperature dependence of the longitudinal sound speed (left) and acoustic relaxation frequency (right).

Published under an exclusive license by AIP Publishing

acoustic relaxation is either too fast or too slow to act on TL signals, while not at intermediate temperatures, where acoustic relaxation is expected to be pronounced. The acoustic bandwidth in the TL is essentially determined by the size of the pump–probe beams and the pulse width. One way to extend the dynamic range could be to play with the pump–probe beam size by introducing an optical zooming system to enable the automatic tuning. In conclusion, the TL geometry used in this work allows extracting the acoustic relaxation in a limited (temperature) dynamic range. To study acoustic relaxation in a broad range, transient grating spectroscopy[48] and nanosecond acoustic interferometry[17] based on a phase mask interferometer[69] are more tangible techniques.

DATA AVAILABILITY

The data that support the findings of this study are available from the corresponding author upon reasonable request.

REFERENCES

[1] C. A. Angell, "Formation of glasses from liquids and biopolymers," Science **267**, 1924 (1995).
[2] M. D. Ediger, C. A. Angell, and S. R. Nagel, "Supercooled liquids and glasses," J. Phys. Chem. **100**, 13200 (1996).
[3] F. Sciortino, "Potential energy landscape description of supercooled liquids and glasses," J. Stat. Mech.: Theory Exp. **2005**, P05015.
[4] A. Widmer-Cooper, H. Perry, P. Harrowell, and D. R. Reichman, "Irreversible reorganization in a supercooled liquid originates from localized soft modes," Nat. Phys. **4**(9), 711 (2008).
[5] L. Berthier and M. D. Ediger, "Facets of glass physics," Phys. Today **69**(1), 40 (2016).
[6] G. B. McKenna and S. L. Simon, "50th anniversary perspective: Challenges in the dynamics and kinetics of glass-forming polymers," Macromolecules **50**, 6333 (2017).
[7] A. Safari, R. Saidur, F. A. Sulaiman, Y. Xu, and J. Dong, "A review on supercooling of phase change materials in thermal energy storage systems," Renewable Sustainable Energy Rev. **70**, 905 (2017).
[8] G. G. Stonehouse and J. A. Evans, "The use of supercooling for fresh foods: A review," J. Food Eng. **148**, 74 (2015).
[9] K. Kothari, V. Ragoonanan, and R. Suryanarayanan, "Influence of molecular mobility on the physical stability of amorphous pharmaceuticals in the supercooled and glassy states," Mol. Pharmaceutics **11**, 3048 (2014).
[10] J. Wong and C. A. Angell, *Glass: Structure by Spectroscopy* (M. Dekker, New York, 1976).
[11] P. K. Dixon, L. Wu, S. R. Nagel, B. D. Williams, and J. P. Carini, "Scaling in the relaxation of supercooled liquids," Phys. Rev. Lett. **65**, 1108 (1990).
[12] U. Bengtzelius, W. Gotze, and A. Sjolander, "Dynamics of supercooled liquids and the glass transition," J. Phys. C: Solid State Phys. **17**, 5915 (1984).
[13] P. G. Debenedetti and F. H. Stillinger, "Supercooled liquids and the glass transition," Nature **410**, 259 (2001).
[14] W. Gotze and L. Sjogren, "Relaxation processes in supercooled liquids," Rep. Prog. Phys. **55**, 241 (1992).
[15] J. C. Dyre, "Colloquium: The glass transition and elastic models of glass-forming liquids," Rev. Mod. Phys. **78**, 953 (2006).
[16] P. Lunkenheimer, U. Schneider, R. Brand, and A. Loid, "Glassy dynamics," Contemp. Phys. **41**, 15 (2000).
[17] T. Hecksher, D. H. Torchinsky, C. Klieber, J. A. Johnson, J. C. Dyre, and K. A. Nelson, "Toward broadband mechanical spectroscopy," Proc. Natl. Acad. Sci. U. S. A. **114**, 8710 (2017).
[18] N. B. Olsen, T. Christensen, and J. C. Dyre, "Time-temperature superposition in viscous liquids," Phys. Rev. Lett. **86**, 1271 (2001).
[19] K. Niss and T. Hecksher, "Perspective: Searching for simplicity rather than universality in glass-forming liquids," J. Chem. Phys. **149**, 230901 (2018).
[20] T. C. Ransom and W. F. Oliver, "Glass transition temperature and density scaling in cumene at very high pressure," Phys. Rev. Lett. **119**, 025702 (2017).
[21] Y. Yang and K. A. Nelson, "T_C of the mode coupling theory evaluated from impulsive stimulated light scattering on Salol," Phys. Rev. Lett. **74**, 4883 (1995).
[22] W. Götze, "The essentials of the mode-coupling theory for glassy dynamics," Condens. Matter Phys. **1**, 873 (1998).
[23] L. M. C. Janssen, "Mode-coupling theory of the glass transition: A primer," Front. Phys. **6**, 97 (2018).
[24] D. Gundermann, U. R. Pedersen, T. Hecksher, N. P. Bailey, B. Jakobsen, T. Christensen, N. B. Olsen, T. B. Schrøder, D. Fragiadakis, and R. Casalini, "Predicting the density-scaling exponent of a glass-forming liquid from prigogine–Defay ratio measurements," Nat. Phys. **7**, 816 (2011).
[25] J.-L. Garden, "Macroscopic non-equilibrium thermodynamics in dynamic calorimetry," Thermochim. Acta **452**, 85 (2007).
[26] N. O. Birge and S. R. Nagel, "Specific-heat spectroscopy of the glass transition," Phys. Rev. Lett. **54**, 2674 (1985).
[27] N. O. Birge, P. K. Dixon, and N. Menon, "Specific heat spectroscopy: Origins, status and applications of the 3ω method," Thermochim. Acta **304-305**, 51 (1997).
[28] N. O. Birge, "Specific-heat spectroscopy of glycerol and propylene glycol near the glass transition," Phys. Rev. B **34**, 1631 (1986).
[29] E. H. Bentefour, C. Glorieux, M. Chirtoc, and J. Thoen, "Thermal relaxation of glycerol and propylene glycol studied by photothermal spectroscopy," J. Chem. Phys. **120**, 3726 (2004).
[30] E. H. Bentefour, C. Glorieux, M. Chirtoc, and J. Thoen, "Broadband photopyroelectric thermal spectroscopy of a supercooled liquid near the glass transition," J. Appl. Phys. **93**, 9610 (2003).
[31] Y. Z. Chua, G. Schulz, E. Shoifet, H. Huth, R. Zorn, J. W. P. Scmelzer, and C. Schick, "Glass transition cooperativity from broad band heat capacity spectroscopy," Colloid Polym. Sci. **292**, 1893 (2014).
[32] C. Bauer, R. Böhmer, S. Moreno-Flores, R. Richert, H. Sillescu, and D. Neher, "Capacitive scanning dilatometry and frequency-dependent thermal expansion of polymer films," Phys. Rev. E **61**, 1755 (2000).
[33] K. Niss, D. Gundermann, T. Christensen, and J. C. Dyre, "Dynamic thermal expansivity of liquids near the glass transition," Phys. Rev. E **85**, 041501 (2012).
[34] I. Chang, F. Fujara, B. Geil, G. Heuberger, T. Mangel, and H. Sillescu, "Translational and rotational molecular motion in supercooled liquids studied by NMR and forced Rayleigh scattering," J. Non-Cryst. Solids **172-174**, 248 (1994).
[35] S. Sastry, P. G. Debenedetti, and F. H. Stillinger, "Signatures of distinct dynamical regimes in the energy landscape of a glass-forming liquid," Nature **393**(6685), 554 (1998).
[36] B. Jakobsen, T. Hecksher, T. Christensen, N. B. Olsen, J. C. Dyre, and K. Niss, "Communication: Identical temperature dependence of the time scales of several linear-response functions of two glass-forming liquids," J. Chem. Phys. **136**, 081102 (2012).
[37] M. Celebrano, D. Rocco, M. Gandolfi, A. Zilli, F. Rusconi, A. Tognazzi, A. Mazzanti, L. Ghirardini, E. A. A. Pogna, and L. Carletti, "Optical tuning of dielectric nanoantennas for thermo-optically reconfigurable nonlinear metasurfaces," Opt. Lett. **46**, 2453 (2021).
[38] M. Terazima and N. Hirota, "Rise profile of the thermal lens signal: Contribution of the temperature lens and the population lens," J. Chem. Phys. **100**, 2481 (1994).
[39] S. E. Bialkowski, *Photothermal Spectroscopy Methods for Chemical Analysis* (John Wiley & Sons, 1996), Vol. 177.
[40] M. Terazima, T. Hara, and N. Hirota, "Population lens in thermal lens spectroscopy. 2. Probe wavelength dependence and a new method for subtracting the transient absorption from the thermal lens signal," J. Phys. Chem. **97**, 10554 (1993).
[41] M. Terazima, "Temperature lens and temperature grating in aqueous solution," Chem. Phys. **189**, 793 (1994).
[42] L. C. Malacarne, N. G. C. Astrath, G. V. B. Lukasievicz, E. K. Lenzi, M. L. Baesso, and S. E. Bialkowski, "Time-resolved thermal lens and thermal mirror spectroscopy with sample–fluid heat coupling: A complete model for material characterization," Appl. Spectrosc. **65**, 99 (2011).

Published under an exclusive license by AIP Publishing

[43]J. Shen, R. D. Lowe, and R. D. Snook, "A model for CW laser induced mode-mismatched dual-beam thermal lens spectrometry," Chem. Phys. **165**, 385 (1992).
[44]M. Gandolfi, G. Benetti, C. Glorieux, C. Giannetti, and F. Banfi, "Accessing temperature waves: A dispersion relation perspective," Int. J. Heat Mass Transfer **143**, 118553 (2019).
[45]J. Schroeder, "Signal processing via Fourier-Bessel series expansion," Digital Signal Process. **3**, 112 (1993).
[46]S. K. Suslov, "Some orthogonal very well poised-functions," J. Phys. A: Math. Gen. **30**, 5877 (1997).
[47]L. S. Garca-Coln, L. F. Del Castillo, and P. Goldstein, "Theoretical basis for the Vogel-Fulcher-Tammann equation," Phys. Rev. B **40**, 7040 (1989).
[48]D. M. Paolucci and K. A. Nelson, "Impulsive stimulated thermal scattering study of structural relaxation in supercooled glycerol," J. Chem. Phys. **112**, 6725 (2000).
[49]D. Kessler and D. Kosloff, "Elastic wave propagation using cylindrical coordinates," Geophysics **56**, 2080 (1991).
[50]M. Gandolfi, F. Banfi, and C. Glorieux, "Optical wavelength dependence of photoacoustic signal of gold nanofluid," Photoacoustics **20**, 100199 (2020).
[51]C. Glorieux, K. Van de Rostyne, J. Goossens, G. Shkerdin, W. Lauriks, and K. A. Nelson, "Shear properties of glycerol by interface wave laser ultrasonics," J. Appl. Phys. **99**, 013511 (2006).
[52]Y. H. Jeong, S. R. Nagel, and S. Bhattacharya, "Ultrasonic investigation of the glass transition in glycerol," Phys. Rev. A **34**, 602 (1986).
[53]I. V. Blazhnov, N. P. Malomuzh, and S. V. Lishchuk, "Temperature dependence of density, thermal expansion coefficient and shear viscosity of supercooled glycerol as a reflection of its structure," J. Chem. Phys. **121**, 6435 (2004).
[54]Y.-X. Yan, L.-T. Cheng, and K. A. Nelson, "The temperature-dependent distribution of relaxation times in glycerol: Time-domain light scattering study of acoustic and mountain-mode behavior in the 20 MHz–3 GHz frequency range," J. Chem. Phys. **88**, 6477 (1988).
[55]S. J. Sheldon, L. V. Knight, and J. M. Thorne, "Laser-induced thermal lens effect: A new theoretical model," Appl. Opt. **21**, 1663 (1982).
[56]J. F. Power, "Pulsed mode thermal lens effect detection in the near field via thermally induced probe beam spatial phase modulation: A theory," Appl. Opt. **29**, 52 (1990).
[57]B. Schiener, R. Böhmer, A. Loidl, and R. V. Chamberlin, "Nonresonant spectral hole burning in the slow dielectric response of supercooled liquids," Science **274**, 752 (1996).
[58]P. Lunkenheimer, A. Pimenov, B. Schiener, R. Böhmer, and A. Loidl, "High-frequency dielectric spectroscopy on glycerol," Europhys. Lett. **33**, 611 (1996).
[59]L. Berthier, G. Biroli, J.-P. Bouchaud, L. Cipelletti, D. El Masri, D. L'Hôte, F. Ladieu, and M. Pierno, "Direct experimental evidence of a growing length scale accompanying the glass transition," Science **310**, 1797 (2005).
[60]R. Richert, "Non-linear dielectric signatures of entropy changes in liquids subject to time dependent electric fields," J. Chem. Phys. **144**, 114501 (2016).
[61]The refractive index of the lens (N-BK7) is 1.5195 at 532 nm and 1.5066 at 1064 nm, respectively. Given the curvature of the lens (LA1314, Thorlabs®) is 64.4 mm, the deviation of the waist position of the two beams could be estimated as ~3 mm with the help of lens maker's equation (n.d.).
[62]M. Gandolfi, L. Liu, P. Zhang, M. Kouyaté, R. Salenbien, F. Banfi, and C. Glorieux, "Revisiting impulsive stimulated thermal scattering in supercooled liquids: Relaxation of specific heat and thermal expansion" (unpublished).
[63]L. A. Roed, J. C. Dyre, K. Niss, T. Hecksher, and B. Riechers, "Time-scale ordering in hydrogen- and van der Waals-bonded liquids," J. Chem. Phys. **154**, 184508 (2021).
[64]R. Salenbien, R. Côte, J. Goossens, P. Limaye, R. Labie, and C. Glorieux, "Laser-based surface acoustic wave dispersion spectroscopy for extraction of thicknesses, depth, and elastic parameters of a subsurface layer: Feasibility study on intermetallic layer structure in integrated circuit solder joint," J. Appl. Phys. **109**, 093104 (2011).
[65]F. Alvarez, A. Alegra, and J. Colmenero, "Relationship between the time-domain Kohlrausch-Williams-Watts and frequency-domain Havriliak-Negami relaxation functions," Phys. Rev. B **44**, 7306 (1991).
[66]K. Schröter and E. Donth, "Viscosity and shear response at the dynamic glass transition of glycerol," J. Chem. Phys. **113**, 9101 (2000).
[67]R. Richert and C. A. Angell, "Dynamics of glass-forming liquids. V. On the link between molecular dynamics and configurational entropy," J. Chem. Phys. **108**, 9016 (1998).
[68]R. Böhmer, K. L. Ngai, C. A. Angell, and D. J. Plazek, "Nonexponential relaxations in strong and fragile glass formers," J. Chem. Phys. **99**, 4201 (1993).
[69]C. Glorieux, J. D. Beers, E. H. Bentefour, K. Van de Rostyne, and K. A. Nelson, "Phase mask based interferometer: Operation principle, performance, and application to thermoelastic phenomena," Rev. Sci. Instrum. **75**, 2906 (2004).

Published under an exclusive license by AIP Publishing